Manipulation of High-Order Scattering Processes in Ultrasmall Optical Resonators to Control Far-Field Emission

Brandon Redding,[1] Li Ge,[2,3] Qinghai Song,[4] Glenn S. Solomon,[5] and Hui Cao[1,*]
[1]Department of Applied Physics, Yale University, New Haven, Connecticut 06520, USA
[2]Department of Engineering Science and Physics, College of Staten Island, CUNY, Staten Island, New York 10314, USA
[3]The Graduate Center, CUNY, New York, New York 10016, USA
[4]Department of Electronic and Information Engineering, Shenzhen Graduate School, Harbin Institute of Technology, Shenzhen, 518055, China
[5]Joint Quantum Institute, National Institute of Standards and Technology and University of Maryland, Gaithersburg, Maryland 20899, USA
(Received 26 September 2013; published 25 April 2014)

By imposing a set of harmonic perturbations to a microcavity boundary, we induce conversion and mixing of orbital angular momentum of light via surface scattering. Multiple scattering paths are available due to high-order scattering, which can be greatly enhanced by quasidegenerate resonances. By manipulating the relative strengths of these scattering processes, we theoretically synthesize the angular momentum spectra of individual modes so as to control their far-field patterns. We demonstrate experimentally that in wavelength-scale cavities of a fixed shape, the neighboring modes can have dramatically different emission directionality. This phenomenon is robust against slight shape deviation and surface roughness, and provides a general mechanism to control the emission direction of ultrasmall resonators.

DOI: 10.1103/PhysRevLett.112.163902 PACS numbers: 42.55.Sa, 42.25.−p, 42.60.Da

High-order processes have been widely studied in many areas of physics, and usually the lower-order effects dominate over the higher-order ones. Here we use optical microcavities as an example to show how to control high-order scattering processes and illustrate their potential advantages. Optical microcavities have a broad range of applications from coherent light sources in integrated photonics, to cavity quantum electrodynamics, and biochemical sensing [1,2]. It is crucial to design cavity resonances with properties suitable for target applications. In this Letter, we consider the far-field emission pattern. In a circular dielectric disk, whispering-gallery (WG) modes are formed by total internal reflection, and their outputs are isotropic. Directional emission is desired for many applications such as microlasers and single-photon emitters. One approach to obtaining directional emission is to deform the disk boundary from a circle. There have been extensive studies on the emission directionality of deformed microcavities; however, most of them explored the emission directions of *known* cavity shapes, e.g., ellipse, quadruple, stadium, spiral, or limacon [3,4]. The inverse problem, i.e., to design the cavity shape to obtain a desired emission pattern, is much more challenging and remains an open question. Moreover, the majority of deformed microcavities that have been studied have a dimension significantly larger than the wavelength; thus, the output directions can be predicted from the escape routes of optical rays from the boundaries [5–18]. As the cavity size approaches the wavelength, the ray model fails, and the output direction is dictated by wave effects [19,20]. Thus the emission directionality is no longer universal; i.e., it varies from one resonance to another. A general treatment of far-field emission and a recipe to control the emission directionality of individual resonances are still missing.

To address these problems, we adopt a general description of the cavity boundary as a sum of harmonic modulations, and predict the far-field pattern of each resonant mode from its angular momentum spectrum. The electromagnetic field of a mode outside the cavity can be decomposed into a set of outgoing waves with well-defined orbital angular momentum, and the emission pattern is determined by the interference of these waves in the far field. In order to control the emission pattern, we will theoretically synthesize the angular momentum spectrum. In a circular dielectric disk, each WG mode has only one angular momentum. By introducing a set of harmonic modulations of the disk boundary, we induce angular momentum conversion and mixing through surface scattering, which can be described by the recently developed perturbation theory [21–24]. Higher-order scattering processes, usually less efficient than lower-order ones, can be resonantly enhanced and play an important role in constructing the angular momentum spectra of microcavity resonances. By manipulating these scattering processes we are able to design the angular momentum spectrum and achieve the desired emission pattern for each individual mode. In particular, we will show in wavelength-scale microcavity lasers that neighboring modes can display

dramatically different output directionality, from unidirectional emission to bidirectional and to unidirectional in the opposite direction, even though the cavity shape and spatial pump profile are kept constant. This work differs from previous ones, where different emission patterns were obtained by modifying the pump profile [25].

Because of strong index guiding of light in the disk plane, a semiconductor microdisk can be treated as a two-dimensional cavity with an effective index of refraction n_{eff}. We consider a GaAs disk surrounded by air with $n_{\text{eff}} = 3.26$. For a general description of the cavity shape, we decompose the disk boundary into harmonic functions in the polar coordinates,

$$\rho(\theta) = R\left[1 + \sum_{\upsilon} \varepsilon_{\upsilon} \cos(\upsilon\theta)\right] \qquad (\upsilon = 2, 3, \ldots), \quad (1)$$

where R is the average radius of the disk and ε_{ν} is the amplitude of the νth harmonic. The dipolar term of $\cos\theta$ is removed by a proper choice of the coordinate origin. Starting from the unperturbed, circular microdisk, a WG mode has a well-defined angular momentum described by the azimuthal number m_0. A harmonic perturbation $\cos(\nu\theta)$ of the disk boundary scatters light from m_0 to $m_0 \pm \nu$, then to $m_0 \pm 2\nu$, and so on. For small ε_{ν}, the additional angular momenta have only a modest effect on the intracavity field profile, but they may have a dramatic effect on the far-field pattern, because the $m < m_0$ components have stronger leakage and can have comparable and even larger amplitudes than the m_0 component outside the cavity.

The amplitudes of the additional angular momentum components depend not only on the strength of the perturbation (ε_{ν}), but also on the spectral overlap between the unperturbed resonance associated with the original angular momentum and the newly generated angular momentum [26]. For example, scattering from m_0 to $m_0 - \nu$ is enhanced when the frequencies of the WG modes with m_0 and $m_0 - \nu$ are well aligned. The spectral overlap can make higher-order scattering processes significant and even comparable to the lower-order ones [27].

The far-field emission pattern of a deformed microdisk with an arbitrary combination of harmonic perturbations can be estimated by first calculating the angular momentum components which are introduced by the perturbations and then considering the interference between these components. Hence, introducing harmonic perturbations to the cavity boundary shape may be used as a "knob" to tune the far-field emission pattern. In previous studies [26,27], we showed theoretically that the emission patterns of deformed microcavities can be varied significantly with the first-order or the second-order perturbations; however, many of these numerical examples required a fine-tuning of the cavity shape, which is difficult to realize experimentally. In this Letter, we use higher-order scattering, which is more tolerant to the limited accuracy of experimental fabrication than lower-order scattering (see the Supplemental Material [28]). In addition, we will control the resonant enhancement effect by lowering the spectral overlap to further improve the robustness. This combination of higher-order scattering with reduced spectral overlap allows us to design a cavity shape with a desired emission pattern which is robust to slight deviations of cavity shape and surface roughness.

To illustrate this approach, we consider a deformed microdisk defined by Eq. (1) with $\varepsilon_2 = -0.069$, $\varepsilon_3 = 0.008$, and $\varepsilon_4 = -0.0014$. These parameters were chosen to facilitate third-order scattering. We focused our analysis on the transverse-electric polarized modes in which lasing usually occurs. We calculated the resonant modes in the passive cavity using the finite difference frequency domain (FDFD) method. Since the cavity shape is symmetric with respect to the horizontal axis [$\rho(-\theta) = \rho(\theta)$], the modes have either even or odd parity. Below we present the even-parity modes, and the odd-parity modes behave similarly. Figures 1(a)–1(c) show the intensity distribution of three neighboring modes with dominant angular momentum component $m_0 = 10$, 11, and 12 inside the cavity. Because of the small perturbations ($|\varepsilon_{2,3,4}| \ll 1$), the spatial profiles of these modes inside the cavity are quite similar to the WG modes of the unperturbed circular cavity, but the far-field patterns, shown in Figs. 1(d)–1(f), are very different. The $m_0 = 10$ mode emits primarily in the 0° direction (forward), while the

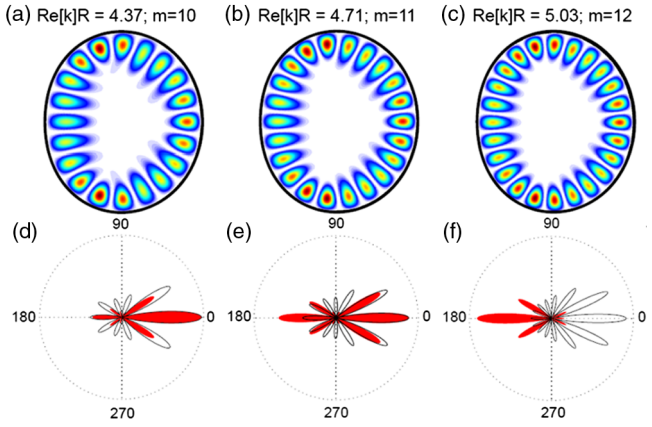

FIG. 1 (color online). Comparison of three neighboring modes in a wavelength-scale cavity which exhibit totally different emission patterns. The cavity boundary is defined by $\rho(\theta) = R[1 - 0.069\cos(2\theta) + 0.008\cos(3\theta) - 0.0014\cos(4\theta)]$. (a)–(c) Intracavity intensity distribution calculated by the FDFD method for the three modes at $kR = 4.37$, 4.71, 5.03. They are similar to whispering-gallery modes with dominant azimuthal number $m_0 = 10$, 11, 12. (d)–(f) Far-field emission pattern for the modes in (a)–(c). The red areas represent the numerical results, and the black solid curves represent the second-order perturbation calculation. The emission direction of these three modes changes from forward ($\theta = 0°$) to bidirectional to backward ($\theta = 180°$), which is not captured by the second-order perturbation treatment, illustrating the importance of higher-order scattering processes.

$m_0 = 11$ mode exhibits bidirectional emission, and the $m_0 = 12$ mode emits in the 180° direction (backward).

To understand why the emission patterns are totally different for three neighboring modes, we calculated their angular momentum spectra inside the cavity by decomposing their field distributions by the Bessel functions, and outside the cavity by the outgoing Hankel functions. For each mode, the relative weight of the lower angular momentum components is larger outside the cavity due to stronger evanescent leakage. The far field ($r \to \infty$) can be expressed as

$$\psi(\theta) = \Sigma_m B_m \cos(m\theta), \qquad m \geq 0. \tag{2}$$

B_m is the coefficient of the angular momentum m. Figures 2(a)–2(c) show the amplitudes of B_m for the three modes. We found that the $m_0 - 5$ component, instead of the m_0 component, is dominant outside the cavity. The $m_0 - 5$ component originates from two second-order scattering processes $m_0 \to m_0 - 2 \to m_0 - 5$ and $m_0 \to m_0 - 3 \to m_0 - 5$ by the $\varepsilon_2 \cos(2\theta)$ and $\varepsilon_3 \cos(3\theta)$ deformations (see the Supplemental Material [28]). The strong spectral overlap of the unperturbed WG modes with m_0 and $m_0 - 3$ enhances the latter process, and makes it stronger than the former.

We applied the second-order perturbation theory derived in Ref. [26] to the $m_0 = 10$, 11, and 12 modes. As shown by the solid curves in Figs. 1(d)–1(f), the second-order perturbation theory effectively captures the forward emission of the $m_0 = 10$ mode but gives a noticeably different far-field pattern for the $m_0 = 11$ mode, and its prediction for the $m_0 = 12$ mode completely deviates from the actual emission pattern. A similar progressing deviation is found for the amplitudes and phases of $B_{m \leq m_0 - 6}$ from $m_0 = 10$ to 12, as shown in Fig. 2. Since the far-field pattern is determined by the interference of the angular momentum components, both their amplitude and phase relations are important. The phase difference between the numerical calculation and the second-order perturbation theory, weighted by the amplitude from the latter, is plotted for each B_m in Figs. 2(d)–2(f). The $m = m_0 - 6$ term stands out as the angular momentum component that displays the most significant phase difference in the $m_0 = 12$ mode. This result suggests that the $m = m_0 - 6$ component plays a key role in flipping the emission direction of the $m_0 = 12$ mode. For further confirmation, we changed the phase of $B_{m_0 - 6}$ given by the second-order perturbation theory to its value in the numerical simulation and found that the emission direction of the $m_0 = 12$ mode was flipped (see the Supplemental Material [28]).

Next, we looked into the $m = m_0 - 6$ component. It comes from five scattering processes: three are second order: $m_0 \to m_0 - 3 \to m_0 - 6$ by the $\varepsilon_3 \cos(3\theta)$ deformation and $m_0 \to m_0 - 2 \to m_0 - 6$, $m_0 \to m_0 - 4 \to m_0 - 6$ by the $\varepsilon_2 \cos(2\theta)$ and $\varepsilon_4 \cos(4\theta)$ deformations; the remaining two are third order: $m_0 \to m_0 - 2 \to m_0 - 4 \to m_0 - 6$ by the $\varepsilon_2 \cos(2\theta)$ deformation and $m_0 \to m_0 - 4 \to m_0 - 8 \to m_0 - 6$ by the $\varepsilon_2 \cos(2\theta)$ and $\varepsilon_4 \cos(4\theta)$ deformations, which are not captured by the second-order perturbation treatment. The strong deviation of the actual $m = m_0 - 6$ coefficient from the value predicted by the second-order perturbation theory clearly shows the importance of the third-order scattering processes. To be more quantitative, we deduced the third-order contribution $B^{(3)}_{m_0-6}$ by subtracting the second-order contribution $B^{(2)}_{m_0-6}$ (calculated by the second-order perturbation theory) from the actual B_{m_0-6} (obtained by numerical simulation). While $B^{(2)}_{m_0-6}$ remains nearly the same for the $m_0 = 10$, 11, and 12 modes, the amplitude of $B^{(3)}_{m_0-6}$ increases nearly 10 times from $m_0 = 10$ to 12 (see the Supplemental Material [28]). Meanwhile, the relative phase between $B^{(2)}_{m_0-6}$ and $B^{(3)}_{m_0-6}$ increases from approximately 90° towards 180°, resulting in destructive interference [28]. Therefore, $B^{(2)}_{m_0-6}$ dominates over $B^{(3)}_{m_0-6}$ in the $m_0 = 10$ mode and $B_{m_0-6} \approx B^{(2)}_{m_0-6} B_{m_0-6} \approx B^{(2)}_{m_0-6}$, while in the $m_0 = 12$ mode $B^{(3)}_{m_0-6}$ becomes dominant, causing a significant change in the phase of B_{m_0-6}.

To explain why the third-order scattering processes become significant in the $m_0 = 12$ mode, we note that the scattering strength is approximately proportional to the amplitude product of each individual process [27]. In this case the dominant third-order process is due to the $\varepsilon_2 \cos(2\theta)$ deformation; its strength is proportional to $|\varepsilon_2|^3 = 3.3 \times 10^{-4}$, which is larger than those of the second-order processes: $|\varepsilon_3|^2 = 6.4 \times 10^{-5}$ and $|\varepsilon_2 \varepsilon_4| = 9.7 \times 10^{-5}$. Thus the cavity shape was designed to favor the

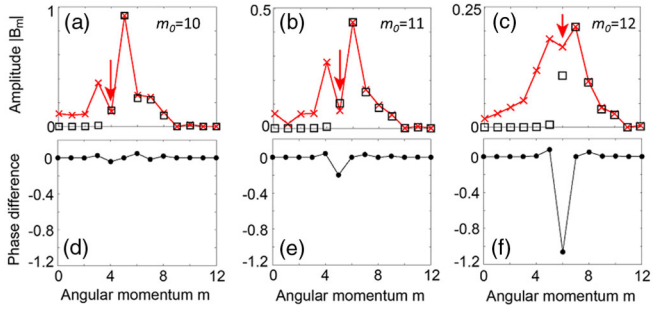

FIG. 2 (color online). Analysis of orbital angular momentum components in the three modes shown in Fig. 1. (a)–(c) Amplitude $|B_m|$ for each angular momentum component, represented by the azimuthal number m, in the far field. The red crosses connected by the solid line represent the numerical results, and the open squares are calculated by the second-order perturbation theory. The arrow marks the $m_0 - 6$ angular momentum component in each mode. (d)–(f) The phase difference of B_m between the numerical simulation and the second-order perturbation theory. The phase change of B_{m_0-6} and its stronger presence in the $m_0 = 12$ mode appear to be responsible for the switch of emission direction.

third-order scattering over the second order, and eliminate the first order ($\varepsilon_6 = 0$). In addition, the scattering strength can be resonantly enhanced due to the spectral overlap of the unperturbed WG modes. Here, the frequency difference Δ between the WG modes of m_0 and $m_0 - 6$ is 0.016 for $m_0 = 12$, much smaller than those for $m_0 = 11$ ($\Delta = 0.061$) and $m_0 = 10$ ($\Delta = 0.062$). Note that the m_0 and $m_0 - 6$ modes have different radial quantum numbers (3 and 1, respectively) allowing their frequencies to be close together. A more accurate measure of the spectral overlap is given in the Supplemental Material [28].

Experimentally, we confirmed the mode-dependent far-field emission from microcavities with the shape described above. GaAs disks of diameter between 1 and 1.5 μm were fabricated by electron-beam lithography and two steps of wet etching [15]. The disks were 265 nm thick and supported by $Al_{0.7}Ga_{0.3}As$ pedestals in the center [28]. InAs quantum dots (QDs) embedded in the GaAs disk were optically excited to provide gain for lasing by a mode-locked Ti:sapphire laser ($\lambda = 790$ nm). We measured the emission spectra and observed the lasing threshold in the emission intensity as a function of pump power. To measure the far-field pattern, we fabricated a ring of radius $\sim$15 μm around each disk to scatter the in-plane emission from the disk out of the plane and imaged the scattered light with a camera [15,28]. An interference filter was placed in front of the camera to select a single lasing mode.

Because of the small cavity size and large mode spacing, the gain spectrum of the InAs quantum dots (QDs) was not broad enough to reach lasing in all three modes ($m_0 = 10$, 11, and 12) in a single disk. Instead, we fabricated a series of microdisks with the same shape, but different radii, so that we could tune the $m_0 = 10$, 11, and 12 modes in separate disks to the center of the QD gain spectrum. Figures 3(a)–3(c) are the top-view SEMs of the three disks. The design shape from Fig. 1 is overlaid on the SEM, confirming that the fabricated disks each had almost the same shape. Slight deviations can be seen, whose effects will be discussed later. The lasing modes correspond to the $m_0 = 10$, 11, and 12 modes shown in Fig. 1. Figures 3(d)–3(f) are the measured far-field patterns, exhibiting the transition from forward to bidirectional to backward emission, in agreement with the calculated emission direction in Fig. 1. In the future, multiple layers of QDs with different size and/or compound composition may be grown in a single wafer to broaden the gain spectrum to cover all three modes in a single disk. One could then select for a specific lasing mode by shaping the optical pump profile or patterning an electrode. Since these modes have different directionality, switching the emission directionality could be realized in a single cavity.

Finally, we discuss the robustness of the emission directionality to surface roughness and slight deviations of the cavity shape. Because of the limited accuracy of the fabrication process, such deviations are unavoidable and vary from disk to disk. Nevertheless, the measured

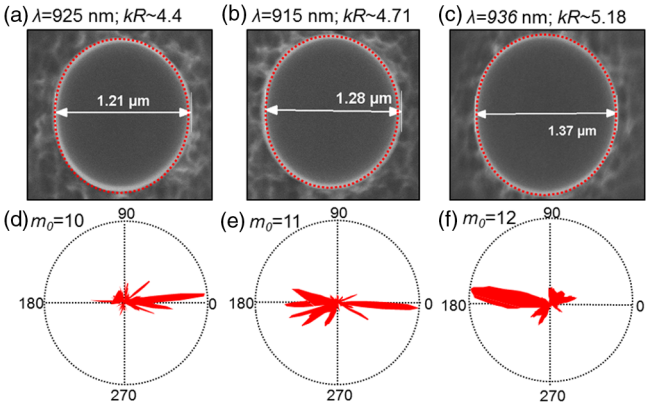

FIG. 3 (color online). Experimental comparison of the emission directionality of lasing modes in three microdisks of the same shape and slightly different size. (a)–(c) SEMs of three microdisks fabricated with the same shape (indicated by the red dotted line). The lasing wavelength, λ, and kR are indicated for each microdisk. (d)–(f) The far-field emission pattern measured for each mode. The emission direction changes from forward to bidirectional to backward for three neighboring modes, in good agreement to the numerical results in Fig. 1.

emission patterns from the three disks in Fig. 3 agree with the theoretical predictions of the design. For further confirmation, we fabricated two more disks of size and shape similar to that in Fig. 3(c). SEM images of these disks are shown in Figs. 4(a) and 4(b), overlaid with the design shape. We achieved lasing in the $m_0 = 12$ mode in both disks, and their far-field pattern are similar to that in Fig. 3(f). To be quantitative, we computed the emission directionality, defined by $U = \int_0^{2\pi} I(\theta)\cos(\theta)d\theta$, where $I(\theta)$ is the far-field intensity as a function of the polar angle θ. As shown in Fig. 4(c), the values of U for the five disks show a clear transition as a function of kR. Furthermore, the three disks supporting lasing in the $m_0 = 12$ mode exhibit similar far-field emission patterns in the backward direction despite the presence of surface

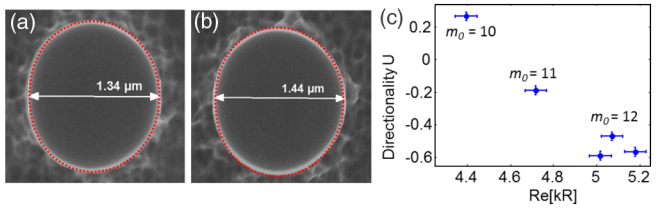

FIG. 4 (color online). Robustness of emission directionality against fabrication error. (a) and (b) SEMs of two microdisks with the same shape as in Fig. 1 (red dotted line) and designed to support lasing in the $m_0 = 12$ mode. The lasing modes are at $kR = 5.02$ and 5.07. Both modes have far-field emission patterns similar to Fig. 3(f). (c) The emission directionality U for five microdisks showing a clear switching of directionality with kR. Furthermore, all three cavities supporting the $m_0 = 12$ mode ($kR \sim 5.1$) show similar emission directionality indicating that the far-field pattern is robust to slight variations in the cavity shape and surface roughness.

roughness which varies for each disk. Hence, the far-field pattern is robust against slight variations of the cavity shape. Such robustness is attributed to the tolerance of high-order scattering processes to fabrication error and the decrease of near-resonance enhancement (see the Supplemental Material [28]).

In summary, we showed that the far-field emission patterns of wavelength-scale microcavities can be varied dramatically by manipulating higher-order scattering processes. The effects of third- and higher-order processes are negligible in most systems in the presence of small perturbations. Even when these effects are significant, previous studies found that these higher order processes produce only modest quantitative differences [29], rather than the dramatic qualitative effect demonstrated here. We attributed this unique phenomenon to the enhancement provided by the underlying quasidegenerate resonances, which is significant in wavelength-scale cavities and gradually disappears in the semiclassical regime [27], where the cavity size is much larger than the wavelength. Unlike four-wave mixing in nonlinear optics, the third-order effect studied here is a linear process that is intensity independent, and it can be easily tuned experimentally. Hence, the wavelength-scale microcavities provide an ideal platform for the study of higher-order processes.

We thank A. Douglas Stone and Jan Wiersig for useful discussions. This work is supported partly by the National Science Foundation under Grants No. ECCS-1068642 and No. ECCS-1128542.

*hui.cao@yale.edu

[1] A. J. Chang and R. K. Campillo, *Optical Processes in Microcavities* (World Scientific, Singapore, 1996).
[2] K. Vahala, *Optical Microcavities* (World Scientific, Singapore, 2004).
[3] T. Harayama and S. Shinohara, Laser Photonics Rev. **5**, 247 (2011).
[4] Y.-F. Xiao, C.-L. Zou, Y. Li, C.-H. Dong, Z.-F. Han, and Q. Gong, Front. Optoelectron. China **3**, 109 (2010).
[5] J. U. Nockel and A. D. Stone, Nature (London) **385**, 45 (1997).
[6] C. Gmachl, F. Capasso, E. E. Narimanov, J. U. Nockel, A. D. Stone, J. Faist, D. L. Sivco, and A. Y. Cho, Science **280**, 1556 (1998).
[7] H. G. L. Schwefel, N. B. Rex, H. E. Türeci, R. K. Chang, A. D. Stone, T. Ben-Messaoud, and J. Zyss, J. Opt. Soc. Am. B **21**, 923 (2004).
[8] S. Shinohara, T. Harayama, H. E. Türeci, and A. D. Stone, Phys. Rev. A **74**, 033820 (2006).
[9] M. Lebental, J. S. Lauret, J. Zyss, C. Schmit, and E. Bogomolny, Phys. Rev. A **75**, 033806 (2007).
[10] S.-B. Lee, J. Yang, S. Moon, J.-H. Lee, K. An, J.-B. Shim, H.-W. Lee, and S. W. Kim, Phys. Rev. A **75**, 011802(R) (2007).
[11] J. Wiersig and M. Hentschel, Phys. Rev. Lett. **100**, 033901 (2008).
[12] S. Shinohara, T. Fukushima, and T. Harayama, Phys. Rev. A **77**, 033807 (2008).
[13] S. Shinohara, M. Hentschel, J. Wiersig, T. Sasaki, and T. Harayama, Phys. Rev. A **80**, 031801(R) (2009).
[14] Q. J. Qang, C. Yan, L. Diehl, M. Hentschel, J. Wiersig, N. Yu, C. Pflügl, M. A. Belkin, T. Edamura, M. Yamanishi, H. Kan, and F. Capasso, New J. Phys. **11**, 125018 (2009).
[15] Q. Song, W. Fang, B. Liu, S.-T. Ho, G. S. Solomon, and H. Cao, Phys. Rev. A **80**, 041807(R) (2009).
[16] C.-H. Yi, M.-W. Kim, and C.-M. Kim, Appl. Phys. Lett. **95**, 141107 (2009).
[17] S. Shinohara, T. Harayama, T. Fukushima, M. Hentschel, T. Sasaki, and E. E. Narimanov, Phys. Rev. Lett. **104**, 163902 (2010).
[18] E. Bogomolny, N. Djellali, R. Dubertrand, I. Gozhyk, M. Lebental, C. Schmit, C. Ulysse, and J. Zyss, Phys. Rev. E **83**, 036208 (2011).
[19] Q. H. Song, L. Ge, A. D. Stone, H. Cao, J. Wiersig, J.-B. Shim, J. Unterhinninghofen, W. Fang, and G. S. Solomon, Phys. Rev. Lett. **105**, 103902 (2010).
[20] B. Redding, L. Ge, Q. Song, J. Wiersig, G. S. Solomon, and H. Cao, Phys. Rev. Lett. **108**, 253902 (2012).
[21] R. Dubertrand, E. Bogomolny, N. Djellali, M. Lebental, and C. Schmit, Phys. Rev. A **77**, 013804 (2008).
[22] S.-W. Ng, P.-T. Leung, and K.-M. Lee, J. Opt. Soc. Am. B **19**, 154 (2002).
[23] J. Lee, S. Rim, J. Cho, and C.-M. Kim, Phys. Rev. Lett. **101**, 064101 (2008).
[24] J. Wiersig, Phys. Rev. A **85**, 063838 (2012).
[25] M. Choi, T. Tanaka, T. Fukushima, and T. Harayama, Appl. Phys. Lett. **88**, 211110 (2006).
[26] L. Ge, Q. Song, B. Redding, and H. Cao, Phys. Rev. A **87**, 023833 (2013).
[27] L. Ge, Q. Song, B. Redding, A. Eberspacher, J. Wiersig, and H. Cao, Phys. Rev. A **88**, 043801 (2013).
[28] See Supplemental Material at http://link.aps.org/supplemental/10.1103/PhysRevLett.112.163902 for a discussion of the second-order perturbation calculations and the robustness of the high-order scattering process to experimental imperfections.
[29] Y. Deng, Q. Lu, Q. Luo, and S. Zeng, Appl. Phys. Lett. **90**, 153902 (2007).